Research Article | Vol. 15, No. 4 / 1 Apr 2024 / Biomedical Optics Express 2308
Biomedical Optics EXPRESS

Tissue mimicking materials and finger phantom design for pulse oximetry

ANDRES J. RODRIGUEZ,[1,*] SANDHYA VASUDEVAN,[2] MASOUD FARAHMAND,[2] SANDY WEININGER,[2] WILLIAM C. VOGT,[2] CHRISTOPHER G. SCULLY,[2] JESSICA RAMELLA-ROMAN,[1] AND T. JOSHUA PFEFER[2]

[1]*Department of Biomedical Engineering, Florida International University, Miami. Florida, 33174, USA*
[2]*Division of Biomedical Physics, Office of Science and Engineering Laboratories, Center for Devices and Radiological Health, Food and Drug Administration, Silver Spring, MD 20993, USA*
[*]*arodr829@fiu.edu*

Abstract: Pulse oximetry represents a ubiquitous clinical application of optics in modern medicine. Recent studies have raised concerns regarding the potential impact of confounders, such as variable skin pigmentation and perfusion, on blood oxygen saturation measurement accuracy in pulse oximeters. Tissue-mimicking phantom testing offers a low-cost, well-controlled solution for characterizing device performance and studying potential error sources, which may thus reduce the need for costly in vivo trials. The purpose of this study was to develop realistic phantom-based test methods for pulse oximetry. Material optical and mechanical properties were reviewed, selected, and tuned for optimal biological relevance, e.g., oxygenated tissue absorption and scattering, strength, elasticity, hardness, and other parameters representing the human finger's geometry and composition, such as blood vessel size and distribution, and perfusion. Relevant anatomical and physiological properties are summarized and implemented toward the creation of a preliminary finger phantom. To create a preliminary finger phantom, we synthesized a high-compliance silicone matrix with scatterers for embedding flexible tubing and investigated the addition of these scatterers to novel 3D printing resins for optical property control without altering mechanical stability, streamlining the production of phantoms with biologically relevant characteristics. Phantom utility was demonstrated by applying dynamic, pressure waveforms to produce tube volume change and resultant photoplethysmography (PPG) signals. 3D printed phantoms achieved more biologically relevant conditions compared to molded phantoms. These preliminary results indicate that the phantoms show strong potential to be developed into tools for evaluating pulse oximetry performance. Gaps, recommendations, and strategies are presented for continued phantom development.

1. Introduction

Oxygen saturation of hemoglobin as measured by pulse oximetry (SpO_2) is an important biological parameter frequently monitored clinically and at-home and point of care [1,2]. Recent work has shown that the photoplethysmography signal used to ascertain SpO_2 is highly sensitive to environmental and physiological sources of noise [3] and is influenced by demographic characteristics. Age, sex, body mass index (BMI), and skin color have been shown to influence the signal [3]. There has been a recent increase in scientific studies presenting evidence that skin pigmentation significantly alters the pulse oximetry signal [4]. This may be detrimental to patients using either clinical-grade systems in a hospital setting or portable devices at home. For example, a retrospective study on 7126 patients with COVID-19 with a total of 32,282 concurrently measured SpO_2 and oxygen saturation levels in arterial blood (SaO_2) showed that SpO_2 values of self-identified Asian, Black, and Hispanic patients were overestimated and higher

#518967 https://doi.org/10.1364/BOE.518967
Journal © 2024 Received 17 Jan 2024; revised 3 Mar 2024; accepted 3 Mar 2024; published 12 Mar 2024

Biomedical Optics EXPRESS

than SaO_2 by an average of 1.33% when compared to White patients, which led physicians to administer lower levels of oxygen [5]. In a follow-up study, researchers confirmed that skin tone can lead to delayed care as pulse oximeters may provide inaccurate readings in individuals of ethnicities that are known to have a higher prevalence of darker skin, affecting the timely administration of necessary treatments [6]. Moreover, researchers found that SpO_2 overestimation increased the risk of hospital readmission regardless of patient race, emphasizing the importance of accurate monitoring.

Pulse oximeters consist of a probe with a light source and a sensor that is typically attached to the fingertip sensor to noninvasively measure the oxygen saturation level, SpO_2, in a person's blood. The device works by emitting two wavelengths of light through the skin and measuring the amount of light absorbed by oxygenated and deoxygenated hemoglobin. This technique isolates the arterial pulse to identify maximally oxygenated blood and consequently provides a quick indication of a person's blood oxygen levels. Several confounding factors can potentially affect pulse oximeter accuracy, and their potential impact is highly dependent on device design and intended use. These factors include variations in performance due to device design parameters (e.g., choice of wavelength and source-detector separation, anatomical site of measurement) and environmental conditions (e.g., ambient light and temperature). Aside from patient demographic characteristics (e.g., skin pigmentation), patient conditions such as motion artifacts from movement, respiratory rate, and venous pulsations may also significantly alter measured PPG signals. The impact of these many conditions on a given optical device may be characterized through bench testing [7] using tissue-mimicking phantoms. These phantoms may be used by device developers to evaluate device performance under well-controlled, adjustable conditions mimicking the variable patient anatomy and physiology. It is important to note that none of the existing phantoms match human volunteer data [7]. Human volunteer testing for medical devices is time-consuming and costly. Evaluating modern materials to create phantoms for pulse oximetry bench testing is a crucial step towards accelerating regulatory approval and facilitating standardization.

A variety of tissue-mimicking materials (TMMs) that may be suitable for testing pulse oximeters have been developed in prior studies with a wide range of applications. Agar gel has been used to craft a finger-shaped phantom with bone-mimicking objects for photoacoustic imaging [8]. A cylindrical phantom, comprising a hemodialysis filter within a gelatin matrix, has been used for 19F MRI oximetry [9]. Researchers working on a 3D vessel detection system with NIR developed a phantom closely resembling human skin tissue using polyacetal resin [10]. Finger phantoms have also been filled with intralipid and red blood cells to replicate human finger properties for glucose monitoring [11,12]. Researchers have explored the development of phantoms using gels and polydimethylsiloxane (PDMS) with varying scattering properties and for studying PPG and oximetry [13,14]. In the flow phantom literature, various materials and blood-mimicking fluids were used for different applications, including ultrasound, CT, MRI, and pulse oximetry. Tuchin et al. developed epoxy resin-based phantoms with capillary networks to simulate fingernail tissue [15]. Phillips et al. [16] used a pulsatile pump to simulate physiological arterial pressure with varying pulse pressure, pumping a saline mixture with black pigment dye through an incompressible silicone tubing enclosed within a glass cuvette, which was used to evaluate electrical and optical sensors. Chen et al. [17] constructed skin layers using gelatin and agar with added components like synthetic melanin, India ink, absorbing dyes, intralipid, bovine serum albumin, and silica microspheres to simulate skin's optical and acoustic properties, embedding vessels for blood mimicking fluid flow, and compared the phantoms to existing in vivo and ex vivo data through various characterization method. The material, geometries, and methods from these many applications can be implemented toward the development of a pulse oximetry phantom.

In recent years, ongoing efforts in international standardization of pulse oximetry and NIRS (e.g., tissue/cerebral oximetry) technologies have grown to include concerns related to confounding

Biomedical Optics EXPRESS

factors such as skin tone [18,19]. The necessity of such standardization has been underscored, advocating for the development of optical phantoms as a solution that offers repeatable and controlled testing environments that are both cost-effective and less time-consuming compared to *in vivo* trials [20]. Complementing this, several researchers have innovated a two-layered phantoms, which, by incorporating whole human blood into a turbid medium, enables the simulation of dynamic oxygen saturation levels ranging from 0 to 100%, thereby mimicking the complex multi-layered tissue structures found *in vivo* and enhancing the fidelity of tissue oximetry testing [13,21]. Further emphasizing the importance of anatomical accuracy, researchers have contributed to the field by formulating solid phantoms that not only replicate the 3D shapes of human organs but also possess the properties necessary for thorough calibration and performance analysis of biomedical optics devices, thus paving the way for more precise and anatomically correct biophotonic applications [22,23].

A variety of phantom-based test methods for pulse oximetry have been described in the literature. Pologe et al. [24] replicated the optical properties of a human finger using a pulsatile glass vessel and a fluid circuit to pump whole human blood while adjusting its oxygen, carbon monoxide, and methemoglobin levels as needed, ensuring that the blood's spectrophotometric properties are preserved. Their phantom was made from a glass cuvette and their tissue simulator had tighter controls which made it easier to stabilize the oxygenated hemoglobin at hypoxic levels. Nwafor et al. [25] created optical phantoms to mimic the optical properties of skin, with gelatin and lipid solutions representing light absorption and scattering in skin tissue. These phantoms incorporated a 0.2% volume of a blood substitute to simulate the volume fraction of whole blood in human skin and were connected to a pulsatile pump for measurements. Jenne et al. [26] fabricated tissue-equivalent phantom for PPG with properties resembling the upper human skin layers, including various types of blood vessels and pulsation capability. This was achieved by adjusting the mechanical properties of the base material and tuning optical properties using titanium dioxide, India ink, and synthetic melanin, and phantom integration into an artificial circulatory system for testing using piezo-actuated double diaphragm pumps. These phantom designs have been essential for advancing medical research and technology by providing controlled testing environments that mimic human tissues and physiology. Several limitations exist among these phantoms, including the inability to replicate physiologic blood pressures and having to use higher pressures due to the rigidity of tubing material [25]. No commercial solution is available besides digital testers, which modulate LEDs to control the recorded light intensity. This article illustrates some of our strategies to fill this knowledge gap.

We aim to design an optical phantom for pulse oximetry at the finger. The design of our system includes the following requirements: (a) the 3D representation of an adult index finger, (b) a pulsating artery embedded within the phantom with appropriate mechanical properties and dimensions, (c) a circulating liquid mimicking blood and its absorption coefficient across a biologically relevant range. Finger geometry, mechanical, and optical properties were evaluated prior to phantom development via an extensive review of published literature. We then demonstrate the construction of tissue phantoms using two manufacturing approaches: additive manufacturing and molding. Lastly, we evaluate key mechanical and optical properties of individual materials and attain PPG signals with some initial phantoms to demonstrate feasibility of the manufacturing approaches.

2. Methods

In designing our pulse oximetry phantoms, we began with a detailed review of the geometric, mechanical, and fluidic properties of the human index finger and identified our design targets. Utilizing CAD models, we developed "U-channel" designs as well as more anatomically realistic finger models derived from MR images. The outer matrix and embedded vasculature of the phantom consisted of PDMS, PVC and silicone tubing. Fabrication was accomplished through

Biomedical Optics EXPRESS

3D printing and molding processes, with material formulations designed to achieve the target optical properties. We validated material properties with standard optical and mechanical characterization approaches before fabricating phantoms that were tested in a PPG flow system to ensure the ability to replicate physiologically relevant waveforms critical for pulse oximetry.

2.1. Pulse oximetry phantoms design

2.1.1. Human finger properties

The literature was surveyed in search of geometric, mechanical, and fluidic properties of the index finger and its arterial blood vessels. Relevant properties from findings are shown in Table 1, which aid the design inputs of our finger model. Examples include values such as those from Blackstone et al., who demonstrate that the human adult finger ranges between 70 to 80 mm in length and 18-20 mm in width [27]. The distance from the finger's distal phalanx to the skin's surface can range between 3.1-6.3 mm [28]. Using a commercial durometer, Falanga et al. measure a Shore OO hardness of 32 ± 3 on the pad of the index finger of healthy individuals. However, values can reach Shore OO hardness of 70 in patients with sclerodema [29].

The index finger has two main arteries running along its length: the digital radial artery and the proper palmar. Klarhöfer et al. used a 3 T MR scanner and notice the diameter changes in the human index finger to a range of 0.8-1.8 mm [30]. The digital mean arterial pressure measured by Nakayama et al. is 80.6 +/- 1.2 mmHg with compliance of 11.44 +/- 0.66×10-5 cm^3/mmHg [38]. No information was found regarding Young's modulus of the digital arteries; thus, we used the coronary and carotid arteries as reference, whose values range from 6-32 MPa and 11.0-17.9, respectively [39].

2.1.2. Three-dimensional designs

Computer-assisted design (CAD) models were generated using SolidWorks 2020 software (Dassault Systèmes, Vélizy-Villacoublay, France). Small "U-channel" designs were created first to test printers' capability of clearing internal channels with small diameters. These were 1×1 cm cylinders with a dome cap at one end to allow channels to loop around (Fig. 1). Each "U-channel" design has three pairs of channels sized 1.0, 1.1, and 1.2 mm in diameter.

In order to create a more anatomically relevant finger, the index finger was isolated from a T1-weighted MR-derived STL file of the hand from the NIH 3D Print Exchange [41] (Model ID: 3DPX-017237, Hegdé et al, accessed 2022). This team created the template by co-registering and averaging 27 images from 21 healthy subjects; while this template provided an anatomical finger model, a clear limitation was the lack of vasculature and other internal components. Using CAD software, a 24 mm x 26 mm x 60 mm rectangular enclosure was placed around the index finger of the hand model (Fig. 2(a)). A cavity was cut out to use as casting (Fig. 2(b)). This same CAD file was used as a template for digitally defining a finger-shaped mesh.

To improve this model, bifurcating blood vessels (Fig. 2(c)), derived from published illustrations shown in Fig. 2(f)) [42] were designed and embedded into the resulting digital mold (Fig. 2(d)). Reference planes parallel to the top and bottom surface of the finger model were created to maintain the tapering angle of the finger, and then a sketch plane with an offset of 6 mm from those surfaces was used to guide the designed channels. Two entry points were created at the proximal end of the finger phantom for connection with flow systems. The channels then bifurcated twice, resulting in 4 loops at the distal tip of the finger that connected the top and bottom branches to complete the circuit. Similar to the "U-channel" samples, 1.0-, 1.1-, and 1.2-mm diameter channels were created to test how well the material behaved with these new bifurcations and angles. This finger design was cut down to a "fingertip" design (Fig. 2(e)) as this was the primary region of interest and interface between the phantom and pulse oximetry sensor.

Biomedical Optics EXPRESS

Table 1. Geometric, Mechanical, and Hemodynamic Properties of the Human Finger

Article	Anatomical Location	Property	Measurement	Instrumentation
Klarhöfer, et al [30]	Finger - index	Hemodynamic	Arterial blood flow velocity:4.9–19 [cm/sec]; Vessel diameter:0.8-1.8 [mm]; Arterial blood flow rate:3.0–26 [ml/min]	3 Tesla MR scanner
Welsh, et al [31]	Human hand	Hemodynamic	Finger systolic blood pressure (FSBPs):59-192 mmHg	Strain-gauge plethysmography
Blackstone, et al [27]	Finger - Index	Geometric	Length: 70-80 [mm]; Width: 18-20 [mm]; Mass: 21-30 [g] (18-year-olds)	NA: Systematic review: source, CHILDATA [32]
Buryanov, et al [28]	Finger - Soft tissues of the distal phalanges	Geometric	Fingertip I-V length: (Distance from tip of bone to skin surface) range of 3.-6.3 [mm]	X-ray images
Laurent, et al [33]	Radial artery (Medium size) at the wrist	Geometric and Mechanical	Arterial internal diameter: 2.50-2.53 [mm]; Intima-media thickness: 0.06-0.40 [mm]: Arterial wall cross section: 2.5-3.8 [mm^2]	Ultrasonic, echo-tracking system coupled to photoplethysmograph (Finapres system)
Tardy, et al [34]	Digital arteries	Mechanical	Diameter as a function of pressure: ~1.31 mm at 7 [kPa] (~52 mmHg) to 1.325 at 15 [kPa] (~ 112 mmHg)	Ultrasound and PPG
Bochmann, et al [35]	Digital arteries	Mechanical	Compliance: 2.76 - 4.03 mL /mmHg per 100 ml tissue	Impedance plethysmography and a finger BP measuring device
Langewouters, et al [36]	Human finger arteries and rat tail	Mechanical	Pressure-diameter relationships: 1-1.5 [mm] in 0-120 [mmHg] (measured at vessel midpoint)	Photoelectric device [37]
Nakayama, et al [38]	Finger	Mechanical	Digital arterial pressure and compliance: 80.6 +/- 1.2 [mmHg], 11.37 +/- 5.9 × 10-6 [cm^3/mmHg]	Fingertip pneumoplethysmograph and a pneumatic cuff
Falanga, et al [29]	Finger - Index and middle	Mechanical	Hardness: Index pad 32 ± 3; Middle finger center pad 39 ± 1	Commercial Shore OO durometer
Yazdi, et al [39]	Carotid and coronary (3.5-9 mm)	Mechanical	Young's Modulus: 11.0-17.9, 6-32 [MPa]	NA: Review paper
Oprişan, et al [40]	Finger	Mechanical	Young's' Modulus: 0.07-0.20 [MPa]	Steel cylinder normal loaded from 0 to 10 N

Biomedical Optics EXPRESS

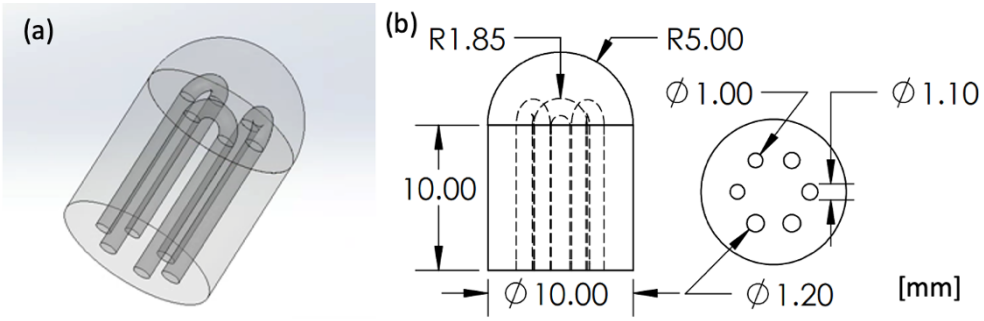

Fig. 1. (a) Isometric view of a sample demonstrating "U-channel" loops at the distal end. (b) Lateral and proximal view demonstrating 3 paired channels of varying diameters.

2.2. Material selection

The phantom was designed to have two major components: the outer matrix and embedded vasculature. Common materials for the outer matrix and their mechanical properties, with PDMS and other silicones being the most widely used (Table 2). A limitation of many of the previously used viscoelastic materials is that they are more stiff than human vasculature. Although room-temperature-vulcanizing silicone typically has a higher Young's modulus than human tissues, Jiang et al. controlled the stiffness by lowering hardener content [7]. Chanda previously experimented with hard (Mold Star 30) and soft (Ecoflex 0010) elastomers in a 2:1 ratio to attain more skin-like properties in molds [43]. Nomoni et al. fabricated custom PDMS vessels with thinner walls than those commercially available by fine-tuning hardener content, curing temperature, and extrusion rates [14]. This resulted in increased compliance of the vessel. Similarly, Sparks et al. combined soft and hard materials, but used 3D printing to create blood vessel mimics with desirable compliance [44]. We will be adapting some of these previously used approaches to test phantom materials and designs that optimally suit the geometric, optical, and mechanical properties of a finger for pulse oximetry.

2.2.1. Casting materials

PDMS is one of the most widely used matrix materials for creating optical phantoms [7]. Its ease of fabrication, durability/stability, optical transparency, and the ability to tune its optical properties with dopants make it an ideal material for fabricating the outer matrix of a pulse oximetry phantom. However, controlling the depth, size, and morphology of wall-less channels is not trivial when casting PDMS. Thus, a generalized approach is to embed circular tubing directly into the mold [15,45–47]. We experimented with various combinations of outer matrix material and embedded tubing to represent vasculature based on materials found in literature (Table 2), specifically with PDMS as outer matrix, and polyvinyl chloride (PVC) and Silicone tubing as vessel mimics.

Based on the literature search and material availability, we fabricated phantoms using Sylgard 184 PDMS with embedded tubing made of silicone (Wacker ELASTOSIL R 407/50 Qosina, NY, USA) or PVC (Continuous-Flex Soft Plastic Tubing, McMaster, IL, USA).

2.2.2. 3D-printing resin

3D printing resins were screened for material properties as shown in Table 3. Optically clear materials are preferable as they enable well-controlled addition of absorbers and scatterers to optimally represent biological media. SLA printers such as the Form 2 and Form 3B (FormLabs, MA, USA) printers have an open resin tank that allows use of customized materials.

Biomedical Optics EXPRESS

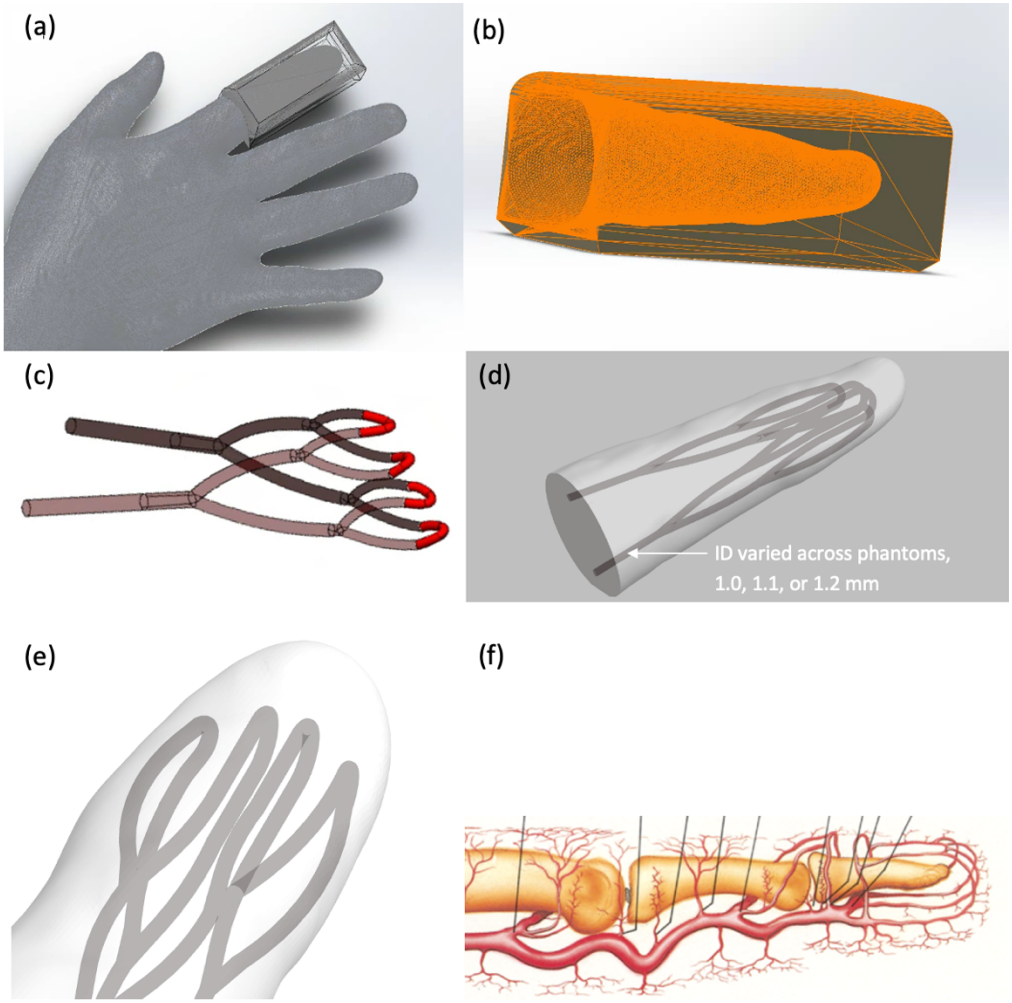

Fig. 2. Workflow to create an anatomically inspired cast and a vascularized finger design. (a) Finger is isolated from the hand model using a rectangular box. (b) Cavity created inside of the box to be used for casting. (c) Vasculature is traced out. (d) Vasculature is embedded into finger design. (e) Finalized fingertip design to be 3D printed and interfaced with pulse oximetry clip-on sensor. (f) Illustration of an arterial system of a finger [42] (reprinted with permission from Elsevier, license number: 5656080231752)

2.3. Optical properties and fabrication

2.3.1. Target optical properties

Target absorption and reduced scattering coefficients were determined by performing a weighted average of layer optical properties in photon-transport models reported in the literature. Chatterjee et al. developed a multilayer anatomical computational model of the index finger to use with Monte Carlo simulations for PPG, which included optical properties of the skin and sublayers, including fat muscle and bone [49]. After we excluded values from the stratum corneum and other epidermis layers, the surrounding matrix, which includes the weighted average of all other skin layers reported in their model, the index finger is expected to have a baseline absorption

Biomedical Optics EXPRESS

Table 2. Mechanical Properties of Casting Materials

Materials	Function	Tensile strength (MPa)	% Elongation at Break	Young's elastic modulus	Hardness
PDMS (Dow Corning, Sylgard 184, Midland, MI)	M-V	7.1	140	200 - 1600 kPa	Medium Stiffness Shore 20A-50A
Ensinger Delrin 150 Homopolymer Acetal (POM)	M-V	75.8	0.25	3.1 GPa	Rockwell R120
Polyester	M	10.0 - 123	0.500 - 2.40%	1.00 - 10.6 GPa	5.00 - 68.0 Barcol (80+ Shore D)
Silastic tubing (Dow Corning, Midland, Michigan)	V	7.1-9.6	568-815	2.1 - 4 MPa	Shore A 50-78
Silicone SILPURAN 2420	M-V	3.5	680%	-	Shore: 12A or 60 00
PTFE	V	20.0 - 35.0	200 - 550%	0.39 - 0.60 GPa	50-65 Shore D
Agar [48]	M	3.25	6.8%	20 GPa	-

M: Matrix; V: Vessel.

Table 3. Mechanical Properties of 3D Printing Materials

Materials	Tensile strength (MPa)	% Elongation at Break	Young's elastic modulus	Shore Hardness
Elastic 50A	3.2-3.7	160%	-	40-50 A
Flexible 80A	3.7-8.9	120%	1.5 MPa	70 A
BioMed Clear Resin	52	0.12%	2080MPa	78 D

coefficient of 0.9 and 1.1 cm^{-1}, while the reduced scattering coefficient should fall near 9.8 and 14.7 cm^{-1} at 660 and 940 nm, respectively.

In order to generate 3D printed samples with specific scattering coefficients, samples of Elastic 50A resin were mixed with TiO_2. To make each of the four batches, increments of TiO_2 from 445 to 612 mg (445, 500, 556, 612 mg), were weighed on a digital balance. A solution of 51 grams of resin and scatterer was mixed in a wide-mouth bottle and vortexed for 1 minute, followed by bath sonication (Model 50D, AQUASONIC, VWR Scientific Products, PA, USA) for 30 minutes to break down any clumps of TiO_2 and ensure homogeneous distribution of scatterer. Using a rotary vane vacuum pump, the solution was degassed in a vacuum chamber at approximately -30 inHg for 30 min. Finally, this stock solution was diluted by a factor of 6 (providing enough resin to fill the printer's print tray) and restirred using a platform rocker (Vari Mix, Model M79735, Thermo Scientific, MA, USA). Given that the print tray (Form 2 Resin Tank LT, FormLabs, MA, USA) needed at least 260 ml, resin was added into the cartridge until it reached 300 ml to account for material losses during the transfer and material used for the print. A series of Elastic 50A resin disc samples 50.8 mm in diameter and 2 mm thick were printed, yielding a volume of 4,054 mm^3. Each batch included 3 discs and, with supports, requires 16.6 ml of resin and 5.5 hours to print. The final concentrations of TiO_2 to Elastic 50A varied from 1.45 to 2.0 mg/g (Table 4).

Biomedical Optics EXPRESS

Table 4. Summary of Optical Samples Fabricated and Scatterer Concentration

Samples (n)	Material	TiO2 Concentration [mg/g]
Print 1 (n = 3)	Elastic 50A	1.5
Print 2 (n = 3)	Elastic 50A	1.6
Print 3 (n = 3)	Elastic 50A	1.8
Print 4 (n = 3)	Elastic 50A	2.0
Batch A (=18)	PDMS	[1.0, 1.1, 1.3, 1.5, 1.7, 1.9]
Batch B (=18)	PDMS	[1.5, 1.7, 1.9, 2.0, 2.2, 2.4]

Molded PDMS samples were fabricated with added TiO_2 as scatterers. First, TiO_2 (ranging from 80 to 130 mg at intervals of 10 mg, depending on the desired concentration) was added to 20 ml glass vials and mixed with 5 grams of PDMS curing agent, vortexed for 1 minute, and sonicated for 30 minutes. Three grams of the curing agent solution were transferred to a larger weighing tray using a 1000 μL pipette to facilitate mixing with the 30-gram PDMS base that would maintain a 10:1 ratio. The mixture was then stirred with a glass rod and degassed for 30 minutes. Lastly, the degassed mixture was slowly poured into the 3D printed casts for pulse oximetry phantoms. For disc phantoms, instead of using 3 grams, 500 mg directly mixed with 5 grams of PDMS in a Petri dish to use as the casts for the 36 optical phantoms (3 phantoms per concentration). Before casting, the PDMS with optical scatterer mixture was stirred with a plastic spatula for approximately 2 minutes each, then degassed for 30 minutes and set on a flat surface to cure for 48 hours. To test the repeatability, three phantoms were created at each scatterer concentration. To test reproducibility, the first 18 phantoms (6 concentrations) – batch A— and the second – batch B— had their 3 respective upper and lower sets of concentrations repeated.

2.3.2. 3D printing

Four characterization samples of Elastic 50A with varying concentrations of scatterer [1.45-2.0 mg/g] were manufactured using the Form2 printer (Table 4). Each batch consisted of 5 dogbones, 3 discs, 2 fingertips, and 3 "U-channel" phantoms. Fingertip and U-channel designs were printed with channel openings facing the resin tank, thus allowing material lodged inside the cavities to drip while printing. Disc and dogbone samples were printed at a 45-degree angle with minimal support to prevent bumps from forming at the imaging surfaces. One alternative is to print samples completely flat on the print plate; however, in this configuration, the material tends to deform around the edges, most likely due to residual stress from peeling it from the build platform. This deformation makes it harder to interface with the flat integrating sphere port, potentially changing the optical measurement and introducing error to Inverse Adding Doubling (IAD) results.

2.3.3. Molding

Several casing designs were 3D printed using Form Clear material. The cases consisted of two halves and a cap (Fig. 3(a)). The halves are clipped together with slots, along with an added aperture on one side to allow the pouring of the silicone mixture and cap to minimize spills during curing. The 1.0 mm inner diameter PVC (McMaster, IL, USA) or 0.8 mm inner diameter silicone (WACKER ELASTOSIL R 407/50, Qosina, NY, USA) tubes were glued in place and cured for 30 minutes. The PDMS mixtures described in Section 2.3.1 were poured slowly beginning at a 45-degree angle and slowly tiling it vertically as it filled to minimize bubble formation, then cured vertically for 48 hours at room temperature. The casing was pried open using a surgical blade and pliers to extract the cured silicone phantom. Male Luer tips were attached to the tubing for connection with either the syringe for patency testing or the pump for PPG validation. The

Biomedical Optics EXPRESS

PDMS molds are approximately 4600 mm^3 in volume. After considering the volume of the silicone and PVC tubing compared to the volume of the casted PDMS, the resulting volume ratios are 0.2% and 0.3%, respectively. The volume ratio is defined as the volume occupied by the hollow channels divided by the total volume of the matrix and channels combined.

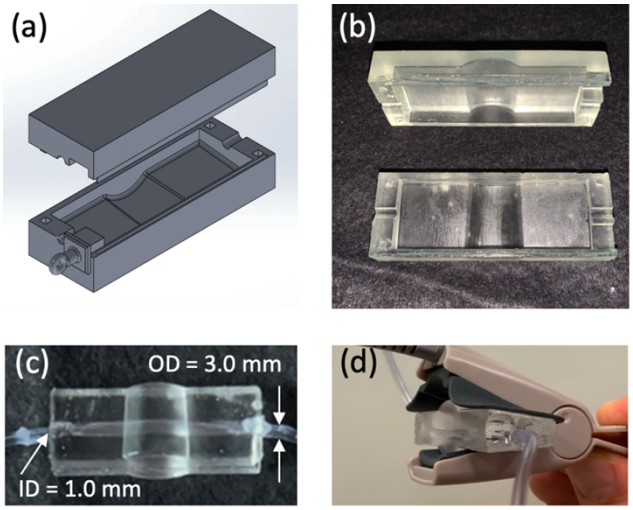

Fig. 3. Demonstration of preliminary phantom fabrication and implementation: (a) CAD model of the cast used to mold pulse oximetry phantom. (b) 3D printed cast made of Form Clear resin. (c) Molded clear PDMS with PVC tube embedded. (d) Fitting of the clip-on pulse oximeter onto the molded PDMS phantom.

2.4. Evaluation and validation methods

2.4.1. Optical properties

Measurement of turbid sample optical properties was accomplished by collecting diffuse reflectance and total transmittance from the characterization samples (disc dimensions: ~50 mm diameter, ~2 mm thick) using a dual-beam spectrophotometer (Lambda 1050, Perkin Elmer, MA, USA). This instrument included a broadband collimated light source and integrating sphere calibrated using a 99% Spectralon reflectance standard (Labsphere, NH, USA). Beam width and sample thickness were measured at the interface using digital calipers. The optical properties were extracted from reflectance and transmittance using the IAD method assuming an anisotropy factor of 0.9 and index of refraction of 1.41 for PDMS and Elastic 50A [50].

2.4.2. Mechanical properties

3D printed dogbone-shaped strips (ASTM D 412-06 (A) [51]) were used for tensile testing on an Instron Universal Testing Machine 33R465 using a 5kN electromechanical load cell (Instron, MA, USA). Dogbone test strips were marked with adhesive stickers (Letraset Letraline Dots) at locations specified by the standard, gripped, displaced at 500 mm/min, and video recorded (Dino-Lite Edge 3.0 AM73915MZTL (R10A), Dino-Lite Digital Microscope, CA, USA), yielding stress vs. strain information used to determine Young's modulus from their elastic regions (determined manually for each sample via visual inspection, and usually within a region of 20% strain or less), whose stress ranged from 0.956-4.97 MPa at maximum load.

Biomedical Optics EXPRESS

2.4.3. Patency testing

Using a syringe and isopropyl alcohol, each channel was tested for continuous flow. To more rigorously assess the printer's capability to generate patent channels, tomographic images were acquired using a micro-CT imaging system (SCANCO Medical AG, Brüttisellen, Switzerland) at 70kVp yielding slices of 10 μm resolution.

2.4.4. Pulse generation and analysis

A Pressure Pulse Generator (Model Number: PPG-601APPG-6014, Flometrics, Inc., CA, USA) with a pressure waveform that represented mean arterial pressure of 90 mmHg, systolic pressure of 122 mmHg, and diastolic pressure of 73 mmHg was used to simulate blood volume change in a finger during PPG signal acquisition. The pulse pressure generator was programmed to generate the arterial pressure waveform for 60 seconds. An 8-second section of the waveform is presented as an example (Fig. 4(a)).

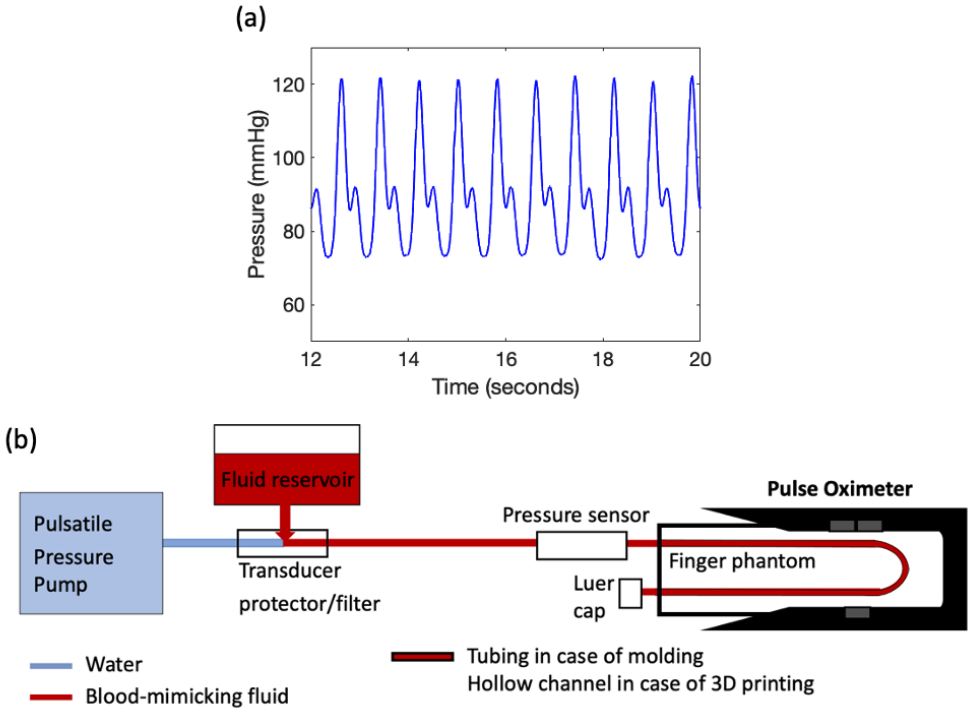

Fig. 4. (a) Input waveform used to drive the pulsatile pressure pump. (b) Experimental setup of instrument and pulse oximetry phantoms used to validate generation of PPG signals.

In order to collect raw optical signal data for both the red and infrared channels, the sensor from a pulse oximeter research module (AFE4490SPO2EVM, Texas Instruments, Inc., TX, USA) was clipped onto the phantoms to detect the PPG signal (Fig. 4(b)). Phantom channels and tubing were filled with blood-mimicking fluid made with water-soluble nigrosin (Sigma-Aldrich, MO, USA) in deionized water, which yield an absorption coefficient of $6.3 \pm 0.1\,\mathrm{cm}^{-1}$ and $1.7 \pm 0.1\,\mathrm{cm}^{-1}$ at 660 and 940 nm, respectively. A transducer protector was added in line to protect the pump from dye particulates (Part # 32104, Qosina, NY, USA). The phantom was capped at one of its outlets to prevent flow. The pump waveform was controlled with a custom MATLAB script. Using a toolbox from Goda et al. [52] raw data was filtered using a 0.5-12 Hz bandpass fourth order Chebyshev filter to compare the quality of the signal across phantom

Biomedical Optics EXPRESS

types. The signal quality index (SQI) uses a PPG waveform beat template [53] and compares the goodness of correlation with the PPG experimental data using a Python implementation of MATLAB's corrcoef() function Lastly, the percent modulation, also known as pulsatility index (PI), was calculated on a 15-second sample of the recording by taking the difference of the maximum and minimum signal, dividing it by the average signal during those 15 seconds, and multiplying it by 100.

3. Results

A total of 108 samples were fabricated and characterized for optical and mechanical properties, patency testing, as well as PPG validation. A summary of the fabrication method used, and type of testing is displayed in Table 5. The resulting turbid phantoms are displayed in Fig. 5.

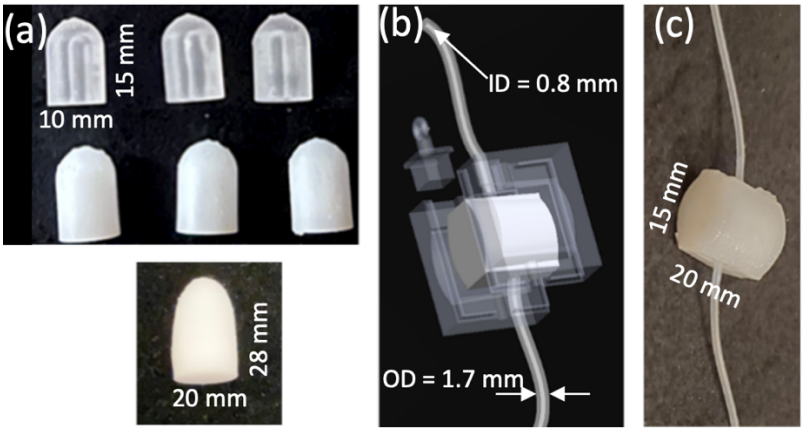

Fig. 5. Resulting pulse oximetry phantoms. (a) Elastic 50A "U-channel" samples that are clear (Top), made turbid with TiO_2 (Middle) and turbid Elastic 50A fingertip phantom with 1.2 mm vessel geometry (Bottom). (b) Final CAD model for mold to perform casting of PDMS. C. TiO_2-doped PDMS phantom with silicone tube.

Table 5. Summary of Samples Fabricated

Samples (n)	Fabrication Method	Testing
Disc (n = 36)	Molding	Optical Properties
Disc (n = 15)	3D-printing	Optical Properties
Dogbone (n = 21)	3D-printing	Tensile
U-channel (n = 18)	3D-printing	Patency
Fingertip (n = 15)	3D-printing	Patency
Fingertip (n = 1)	3D-printing	PPG Validation
Embedded Tube (n = 2)	Molding	PPG Validation

Clear Elastic 50A "U-channel" phantoms are approximately 1,047 mm^3 in volume. The channels are 68.6 mm^3 in volume, thus simulating a 6.6% blood volume fraction. Each batch printed with added supports consumes 5.0 ml of resin, with an estimated print time of 2.75 hours. Clear Elastic 50A fingertip prints are approximately 4,459 mm^3 in volume. Vasculature designs with 1.0-, 1.2-, and 1.4-mm nominal diameters resulted in 3.3-, 4.7-, and 6.4% volume fractions, respectively. Including support material, each phantom consumes roughly 6.2 ml of resin, with an estimated print time of 3.5 hours.

Biomedical Optics EXPRESS

3.1. Optical properties results

The relationship between the measured μ_s' values at two common pulse oximeter wavelengths (660 nm and 940 nm) and TiO_2 concentration is shown in Fig. 6. for total of 36 molded and 12 3D printed phantoms. For PDMS, the range of μ_s' lies between 11.3 and 30.6 cm^{-1} for 660 nm, and between 7.7 and 19.7 cm^{-1} for 940 nm. For Elastic 50A, the range of μ_s' lies between 5.8 and 16.4 cm^{-1} for 660 nm, and between 4.1 and 11.9 cm^{-1} for 940 nm.

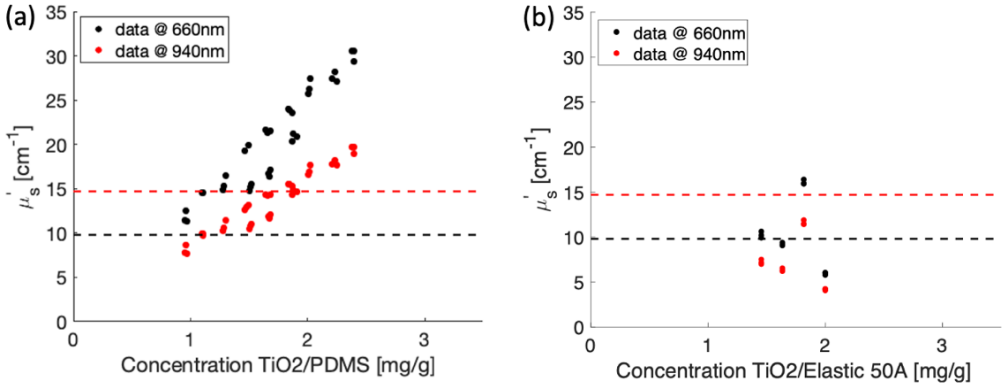

Fig. 6. Reduced scattering coefficient versus concentration of added TiO_2 for (a) PDMS molded circular phantoms and (b) 3D printed discs of Elastic 50A at 660 and 940 nm. Dashed horizontal lines represent target values for mimicking a finger [49].

3.2. Mechanical properties results

Figure 7(a) shows Young's modulus for 3D-printed samples that were placed in a UV-curing oven at 60°C for 20 minutes and samples not exposed to heat or UV curing. Figure 7(b) shows the relationship between Young's modulus and concentration of TiO_2 scatterer. Samples that were UV-cured demonstrated a larger variation than non-cured ones. Mean differences were insignificant across levels of the reduced scattering coefficient.

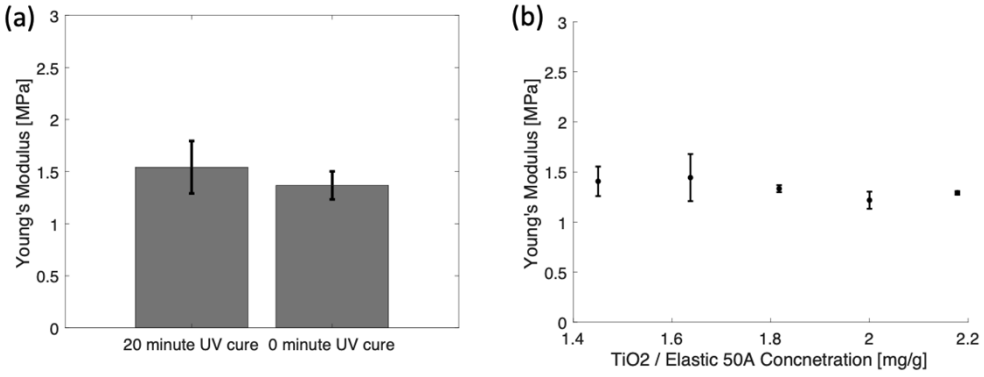

Fig. 7. Tensile testing results of Elastic 50A dogbone samples show the calculated Young's modulus as a function of (a) UV curing time; and (b) TiO_2 concentration.

Biomedical Optics EXPRESS

3.3. Patency tests

Patency test results from the U-channel samples for nominal inner diameters (ID) of 1.0, 1.1, and 1.2 mm are shown in Table 6. Some channels were fully open, while others were fully or partially blocked. The first two prints were identical in preparation and 3D printing settings, although for the second print U-channel samples were UV-cured for 20 minutes whereas no curing was used in the first print. The second print batch had more instances of open 1.1 mm channels than the first, so no curing was implemented in print attempts with added scatterer.

Table 6. Patency Tests Results in U-channel Samples

Print Attempts	Channel ID (mm)	Sample 1	Sample 2	Sample 3	Single-channel Patency
Elastic 50A UV-Cured	1.0	Blocked	Blocked	Blocked	
	1.1	Blocked	Blocked	Blocked	
	1.2	Open	Open	Open	
Elastic 50A	1.0	Blocked	Blocked	Partial	
	1.1	Open	Blocked	Open	
	1.2	Open	Blocked	Open	
Elastic 50A + TiO2 #1	1.0	Blocked	Blocked	Partial	
	1.1	Open	Open	Open	
	1.2	Open	Open	Open	
Elastic 50A + TiO2 #2	1.0	Blocked	Blocked	Blocked	
	1.1	Blocked	Blocked	Blocked	
	1.2	Open	Open	Open	
Elastic 50A + TiO2 #3	1.0	Blocked	Blocked	Blocked	
	1.1	Blocked	Blocked	Blocked	
	1.2	Open	Open	Open	
Elastic 50A + TiO2 #4	1.0	Blocked	Blocked	Partial	
	1.1	Blocked	Blocked	Blocked	
	1.2	Open	Blocked	Blocked	

Patency testing results for the fingertip geometry phantoms are shown in Table 7. The circular symbol indicates the level of patency on the left and right sides of the phantom, while colors indicate whether the phantoms could be used for pulse oximetry testing. Red blocks denote phantoms that are unusable due to blockages during printing or ruptures during post-processing,

Biomedical Optics EXPRESS

while green denotes a viable phantom. The yellow cell represents a case where only the right side of the phantom demonstrated continuous flow.

Table 7. Patency Test Results in 3D Printed Fingertip Phantoms

Print Attempts	Inner Diameter (ID)			Bifurcating-channel Patency
	1.0 mm	1.1 mm	1.2 mm	
Elastic 50A	◉ ◉	⊛ ⊛	◎ ◎	◎ Fully open
Elastic 50A + TiO2 #1	◉ ◉	⊛ ⊛	⊛ ◎	◉ Fully closed
Elastic 50A + TiO2 #2	◉ ◉	⊛ ⊛	⊛ ⊛	⊛ Channel reduction
Elastic 50A + TiO2 #3	◉ ◉	⊛ ⊛	⊛ ⊛	
Elastic 50A + TiO2 #4	◉ ◉	◉ ◉	◉ ⊛	

3.4. PPG validation

Raw signals recorded from the pulse oximetry sensor are shown in Fig. 8. Signals were recorded for a minimum of 1 minute, although only 15 seconds were analyzed for SQI and PI calculations. It is important to note that the pulsatility occurs in the millivolt range and is two orders of magnitude from the mean of the signal. Hence the range of the y axis differs for each phantom. Table 8. shows the resulting SQI values.

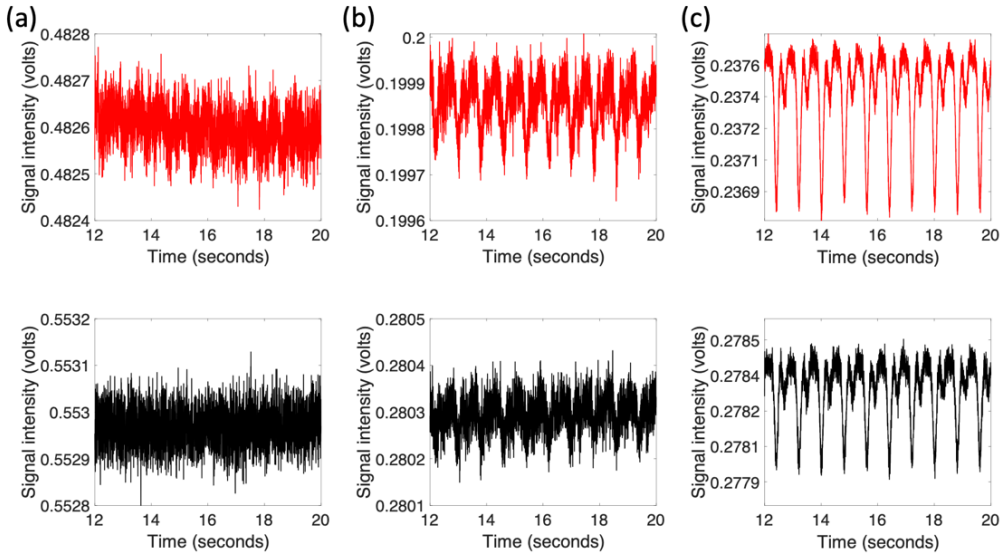

Fig. 8. PPG signal recordings in the red 660 nm (top row) and infrared 940 nm (bottom row) channels while pumping blood mimicking fluid through (a) a molded PDMS turbid phantom with silicone tubing; (b) a molded PDMS turbid phantom with PVC tubing; and (c) a 3D-printed Elastic 50A turbid fingertip phantom with tube-less channels.

Biomedical Optics EXPRESS

Table 8. Mean PPG Signal Quality Index

	PDMS + SI	PDMS + PVC	ELASTIC 50A
RED LED (660 nm)	69.7%	85.9%	98.6%
IR LED (940 nm)	34.8%	81.3%	89.5%

A typical quality metric for pulse oximetry in human data is the percent modulation or pulsatility index (PI), sometimes considered the gold standard of PPG signal quality assessment [54]. PI is the difference between the lowest and highest value of the signal, divided by the signal average, and multiplied by 100%. The PI values in humans have a wide range and can vary from 0.02% to 20% [55]. We recorded a PPG signal on the fabricated phantoms and compared their PI values (Table 9). It is evident that the PI values are much lower for these phantoms, when compared to published human data. However, the molded PDMS + PVC and 3D printed Elastic 50A phantoms demonstrate PI values equal to or higher than 0.02%.

Table 9. Pulsatility Index for Phantoms

	PDMS + SI	PDMS + PVC	ELASTIC 50A
RED LED	0.01%	0.02%	0.05%
IR LED	0.01%	0.02%	0.03%

4. Discussion

There is a strong need to develop phantoms to avoid testing on human subjects which are costly, time consuming, and may not span the parameter space possible with a bench test method. The work presented here provides insight into the development of a phantom, or set of phantoms, that could be implemented in such a test. Our exploration into the complex design and material selection of these phantoms demonstrates their potential to emulate the varied geometries and mechanical properties of human tissue, which is critical for the accurate assessment of pulse oximetry devices. The balance between anatomical realism and fabrication feasibility has been carefully navigated, presenting phantoms that can interface with existing clinical equipment while still presenting the necessary optical and mechanical properties to simulate real-world conditions. Despite some limitations in printing resolution affecting vascular network accuracy, our findings offer a blueprint for future enhancements. Such advancements in phantom technology promise to refine the calibration and testing of pulse oximeters.

Phantoms for pulse oximetry can be designed in many shapes and sizes, and as is common with models there is a need to balance realism and complexity with fabrication simplicity and reproducibility. Few phantoms in the literature take the actual shape of a human finger, but similar cylindrical tapered geometries of relevant size may be ideal as they will enable the phantom to interface with clip-on transmission-mode probes as demonstrated in Fig. 3(d). It is possible that somewhat greater morphological complexity will be needed to simulate clinical performance. Our work has shown that 3D printing and molding may be a useful tool for fabricating phantoms with realistic vascular networks. However, the inability of the tested printers to reliably generate vessels of 1 mm diameter or less may be a significant limiting factor.

The resin manufacturer for Elastic 50A did not provide information on mechanical properties as a function of time in a UV-curing oven. As shown in Fig. 7(a), no significant difference in elasticity was seen between samples that received the recommended 20 minutes of UV-curing from the manufacturer, and samples without any UV-curing. Thus, we continued the assessment of mechanical properties on samples that did not receive UV curing. Differences in mechanical properties can be expected not just as a function of UV exposure, but also as a function of curing temperature, as with PDMS [56,57]. Although the manufacturer recommends curing at

Biomedical Optics EXPRESS

60°C, future work should explore the materials' mechanical and optical property sensitivity to temperature changes. Results in Fig. 7(b) demonstrate that adding TiO_2 as a scatterer will not affect the elasticity of the material. Thus, one can expect similar behaviors inside the printed blood vessels of a pulse oximeter phantom when using a range of scattering concentrations (1.5 x10-3 - 2.2 × 10-3 [g/g]) which yield Young's modulus of 1.22-1.44 MPa. These values are within the expected range for blood vessels such as the carotid artery [39].

The manufacturer of Elastic 50A claims print resolutions down to 100 mm and recommends printing hole diameters of 800 mm or larger. During preliminary testing of a set of U-channel samples with ID channel size of 0.7, 0.8, and 0.9 mm, this material did not demonstrate patency in any channel. Results in Table 6. show no clear correlation between scatterer concentration, and channel patency. The 1.2 mm ID U-channel samples had the highest prevalence of fully open channels, yielding a conclusion that channels of less than 1.2 mm could not be consistently printed using our current setup.

Patency results in Table 7. show that left and right channels were always blocked in the 1 mm diameter case. Channels with ID = 1.1 mm were open with none or little concentration of TiO_2. However, larger TiO_2 concentrations #2-4 (1.6, 1.8, and 2.0 mg/g) demonstrated channel narrowing and blockages. The optimal vessel diameter for the fingertip geometry was 1.2 mm, where flow was unobstructed at lower TiO_2 concentrations, but blocked at higher values. The higher concentrations have a larger probability of preventing the printer's laser from curing the resin around the channel walls as well as preventing patency near the bifurcations of the fingertip phantoms. However, it remains unclear whether the larger concentration of TiO_2 is causing the blockages, especially since the reduced scattering coefficient did not monotonically increase in 3D printed optical phantoms. The linearity noted in molded PDMS samples (Fig. 6(a)) was not achieved with the Elastic 50A (Fig. 7(b)). Residual TiO_2 in the wide-mouth bottle after transferring to the resin cartridge likely led to a degree of inconsistency in μ_s' values.

PPG validation of the three types of phantoms (two molded and one 3D printed) demonstrate the merit of a 3D printing approach. The molded PDMS phantoms with silicone tubing showed the poorest quality signal in both red and IR. Even though silicone showed better compliance than PVC, its inner diameter was smaller by 200 µm, which most likely led to its low performance in SQI and PI. Using PVC tubing helped improve the quality of the signal, especially in the red channels, where it is comparable to the signal for the IR channel in the 3D printed fingertip phantom.

Our current phantom is a promising prototype for pulse oximetry testing, yet it needs refinement to fully emulate the clinical setting. Our study set up did not allow for the calculation of SpO_2 from the fabricated phantoms. The addition of absorbers to the outer matrix in conjunction to perfusing small 3D printed channels with real oxygenated blood better resembles baseline and dynamic oxygenated tissues and enables the calculation of SpO_2 values expected in human subjects. Improvements will focus on enhancing 3D printing resolution for finer vascular structures by exploring different resins and 3D printing technologies. Although TiO_2 as a scatterer in the outer matrix and water-soluble nigrosin as an absorber in the vessels proved to be sufficient in the preliminary pulsatility tests required for PPG signal detection, future pulse oximetry experiments could be enhanced by incorporating both static and dynamic absorption values that mimic real tissue. For example, via the addition of a thin epidermal-mimicking layer like those used by Afshari et al. [13] and exploring alternative blood-mimicking fluids, like those used by Sudakou et al. [21].

5. Conclusion

We have presented a manufacturing and validation process for pulsatile optical phantoms aimed at testing photoplethysmographers and pulse oximeters. Our approach utilized common materials and instrumentation that may be found in many research laboratories, such as PDMS and

Biomedical Optics EXPRESS

photopolymer resin, facilitating the manufacturing of optical phantoms and testing on clip-on pulse oximetry sensors. Our work was able to achieve reliable optical scattering relevant to biological tissues for casted phantoms. In the 3D-printed phantoms, the mechanical properties, specifically Young's modulus, were unaffected by the addition of titanium dioxide. Patency tests show unobstructed manufactured vasculature inner diameter channels equal to or larger than 1.2 mm and 0.8 mm for 3D printed and molded phantoms, respectively. Lastly, we observed a better PPG signal from the 3D-printed compared to the molded phantoms.

Overall, this research highlights the benefits and challenges associated with the 3D printing and molding of phantoms for pulse oximetry. Our findings on fabrication processes, material selection, and optical properties may help inform future pulse oximetry phantom development. By incorporating absorbers and potentially creating thin epidermal layers it may be possible to further advance these test methods. We hope these findings serve as a stepping-stone to characterize sources of inaccuracies in pulse oximetry and to facilitate benchtop testing, thereby reducing the need for costly human studies and improve the state of sensor design.

Funding. National Science Foundation (1648451).

Acknowledgements. We are thankful for the National Science Foundation Engineering Research Center for Precise Advanced Technologies and Health Systems for Underserved Populations (PATHS-UP) (#1648451). This work was funded by an NSF Non-Academic Research Internships for Graduate Students (INTERN) award. A special thank you is given to Anant Agrawal, Achyut Raghavendra, Vivek Palepu, and Zixin Wang (from the Division of Biomedical Physics at FDA); Bryan Ibarra, Matt Schwerin (from Division of Applied Mechanics at FDA); Ajmal Ajmal and Tananant "Mel" Boonya-ananta (from Medical Photonics Laboratory at Florida International University).

The mention of commercial products, their sources, or their use in connection with material reported herein is not to be construed as either an actual or implied endorsement of such products by the Department of Health and Human Services. This article reflects the views of the authors and should not be construed to represent FDA's views or policies.

Disclosures. The authors declare no conflicts of interest.

Data availability. Data underlying the results presented in this paper are not publicly available at this time but may be obtained from the authors upon reasonable request.

References

1. M. A. Almarshad, M. S. Islam, S. Al-Ahmadi, *et al.*, "Diagnostic features and potential applications of PPG signal in healthcare: A systematic review," Healthcare **10**(3), 547 (2022).
2. M. Elgendi, R. Fletcher, Y. Liang, *et al.*, "The use of photoplethysmography for assessing hypertension," NPJ Digit Med **2**(1), 60 (2019).
3. J. Fine, K. L. Branan, A. J. Rodriguez, *et al.*, "Sources of inaccuracy in photoplethysmography for continuous cardiovascular monitoring," Biosensors **11**(4), 126 (2021).
4. A. M. Cabanas, M. Fuentes-Guajardo, K. Latorre, *et al.*, "Skin pigmentation influence on pulse oximetry accuracy: a systematic review and bibliometric analysis," Sensors **22**(9), 3402 (2022).
5. A. Fawzy, T. D. Wu, K. Wang, *et al.*, "Racial and ethnic discrepancy in pulse oximetry and delayed identification of treatment eligibility among patients with COVID-19," JAMA Intern Med **182**(7), 730–738 (2022).
6. A. Fawzy, T. D. Wu, K. Wang, *et al.*, "Clinical outcomes associated with overestimation of oxygen saturation by pulse oximetry in patients hospitalized with COVID-19," JAMA Netw Open **6**(8), e2330856 (2023).
7. B. W. Pogue and M. S. Patterson, "Review of tissue simulating phantoms for optical spectroscopy, imaging and dosimetry," J. Biomed. Opt. **11**(4), 041102 (2006).
8. S. K. Biswas, P. van Es, W. Steenbergen, *et al.*, "A new approach to depict bone surfaces in finger imaging using photoacoustic tomography," in *Photons Plus Ultrasound: Imaging and Sensing 2015*(SPIE 2015), pp. 322–327.
9. J. Vandecasteele, L. Colman, W. De Neve, *et al.*, "An oxygen-consuming phantom simulating perfused tissue to explore oxygen dynamics and 19F MRI oximetry," Magn Reson Mater Phy **23**(4), 217–226 (2010).
10. Y. Mizuno, T. Katayama, and E. Nakamachi, "Development of an accurate 3D blood vessel searching system using NIR light," in *Advanced Biomedical and Clinical Diagnostic Systems VIII* (SPIE 2010), pp. 22–29.
11. A. Srivastava, M. K. Chowdhury, S. Sharma, *et al.*, "Optical clearance effect determination of glucose by near infrared technique: An experimental study using an intralipid based tissue phantom," International Journal of Advances in Engineering & Technology **6**, 1097 (2013).
12. O. Amir, D. Weinstein, S. Zilberman, *et al.*, *Continuous Noninvasive Glucose Monitoring Technology based on "Occlusion Spectroscopy"*, (SAGE Publications, 2007).
13. A. Afshari, R. B. Saager, D. Burgos, *et al.*, "Evaluation of the robustness of cerebral oximetry to variations in skin pigmentation using a tissue-simulating phantom," Biomed. Opt. Express **13**(5), 2909–2928 (2022).
14. M. Nomoni, J. M. May, and P. A. Kyriacou, "Fabricating novel PDMS vessels for phantoms in photoplethysmography investigations," Annu Int Conf IEEE Eng Med Biol Soc **2020**, 4458–4461 (2020).

Biomedical Optics EXPRESS

15. V. V. Tuchin, A. Bashkatov, E. Genina, *et al.*, "Finger tissue model and blood perfused skin tissue phantom," in *Dynamics and Fluctuations in Biomedical Photonics VIII* (SPIE 2011), pp. 169–179.
16. J. P. Phillips, M. Hickey, and P. A. Kyriacou, "Evaluation of electrical and optical plethysmography sensors for noninvasive monitoring of hemoglobin concentration," Sensors **12**(2), 1816–1826 (2012).
17. A. I. Chen, M. L. Balter, M. I. Chen, *et al.*, "Multilayered tissue mimicking skin and vessel phantoms with tunable mechanical, optical, and acoustic properties," Med. Phys. **43**(6Part1), 3117–3131 (2016).
18. I. O. f. Standardization, "ISO 80601-2-61:2017. Medical electrical equipment — Part 2-61: Particular requirements for basic safety and essential performance of pulse oximeter equipment," (2017).
19. I. O. f. Standardization, "ISO 80601-2-85:2021. Medical electrical equipment — Part 2-85: Particular requirements for the basic safety and essential performance of cerebral tissue oximeter equipment," (2021).
20. C. Hornberger and H. Wabnitz, "Approaches for calibration and validation of near-infrared optical methods for oxygenation monitoring," Biomedical Engineering/Biomedizinische Technik **63**(5), 537–546 (2018).
21. A. Sudakou, H. Wabnitz, A. Liemert, *et al.*, "Two-layered blood-lipid phantom and method to determine absorption and oxygenation employing changes in moments of DTOFs," Biomed. Opt. Express **14**(7), 3506–3531 (2023).
22. S. K. V. Sekar, A. Pacheco, P. Martella, *et al.*, "Solid phantom recipe for diffuse optics in biophotonics applications: a step towards anatomically correct 3D tissue phantoms," Biomed. Opt. Express **10**(4), 2090–2100 (2019).
23. D. Burgos, B. Blumenkopf, A. Afshari, *et al.*, "Biomimetic tissue phantoms for neurosurgical near-infrared fluorescence imaging," Neurophoton. **10**(01), 015007 (2023).
24. J. A. Pologe, D. H. Arnold, and T. P. Delianides, "Multi-analyte calibration and verification of a multi-parameter laser-based pulse oximeter," J Clin Monit Comput **36**(2), 579–586 (2022).
25. C. I. Nwafor, K. D. Plant, D. R. King, *et al.*, "Assessment of a noninvasive optical photoplethysmography imaging device with dynamic tissue phantom models," J. Biomed. Opt **22**(09), 1–9 (2017).
26. S. Jenne and H. Zappe, "Multiwavelength tissue-mimicking phantoms with tunable vessel pulsation," J. Biomed. Opt. **28**(04), 045003 (2023).
27. J. M. Blackstone, "Children and gender-differences in exposure and how anthropometric differences can be incorporated into the design of computer input devices," Scandinavian Journal of Work, Environment & Health, 26 (2007).
28. A. Buryanov and V. Kotiuk, "Proportions of hand segments," Int. J. Morphol. **28**(3), 755–758 (2010).
29. V. Falanga and B. Bucalo, "Use of a durometer to assess skin hardness," J. Am. Acad. Dermatol. **29**(1), 47–51 (1993).
30. M. Klarhöfer, B. Csapo, C. Balassy, *et al.*, "High-resolution blood flow velocity measurements in the human finger," Magn. Reson. Med. **45**(4), 716–719 (2001).
31. A. J. Welsh and M. J. Griffin, "Normal values for finger systolic blood pressures in males and females," Int. Arch. Occup. Environ. Health **81**(5), 625–632 (2008).
32. B. Norris and J. R. Wilson, *Childata: The Handbook of Child Measurements and Capabilities: Data for Design Safety* (Consumer Safety Unit, Department of Trade and Industry, 1995).
33. S. Laurent, X. Girerd, J.-J. Mourad, *et al.*, "Elastic modulus of the radial artery wall material is not increased in patients with essential hypertension," Arterioscler. Thromb. **14**(7), 1223–1231 (1994).
34. Y. Tardy, J. Meister, F. Perret, *et al.*, "Non-invasive estimate of the mechanical properties of peripheral arteries from ultrasonic and photoplethysmographic measurements," Clin. Phys. Physiol. Meas. **12**(1), 39–54 (1991).
35. R. Bochmann, U. Reuter, A. List, *et al.*, "Compliance of the digital artery is decreased in patients with essential hypertension," J. Hum. Hypertens. **9**, 627–631 (1995).
36. G. J. Langewouters, A. Zwart, R. Busse, *et al.*, "Pressure-diameter relationships of segments of human finger arteries," Clin. Phys. Physiol. Meas. **7**(1), 43–55 (1986).
37. A. Schabert, R. Bauer, and R. Busse, "Photoelectric device for the recording of diameter changes of opaque and transparent blood vessels in vitro," Pflugers Arch. **385**(3), 239–242 (1980).
38. R. Nakayama and T. Azuma, "Noninvasive measurements of digital arterial pressure and compliance in man," American Journal of Physiology-Heart and Circulatory Physiology **233**(1), H168–H179 (1977).
39. S. G. Yazdi, P. Geoghegan, P. Docherty, *et al.*, "A review of arterial phantom fabrication methods for flow measurement using PIV techniques," Ann. Biomed. Eng. **46**(11), 1697–1721 (2018).
40. C. Oprişan, V. Cârlescu, A. Barnea, *et al.*, "Experimental determination of the Young's modulus for the fingers with application in prehension systems for small cylindrical objects," in *IOP Conference Series: Materials Science and Engineering* (IOP Publishing 2016), p. 012058.
41. M. F. Coakley, D. E. Hurt, N. Weber, *et al.*, "The NIH 3D print exchange: a public resource for bioscientific and biomedical 3D prints," 3D printing and additive manufacturing **1**(3), 137–140 (2014).
42. B. Strauch and W. de Moura, "Arterial system of the fingers," The Journal of hand surgery **15**(1), 148–154 (1990).
43. A. Chanda, "Biomechanical modeling of human skin tissue surrogates," Biomimetics **3**(3), 18 (2018).
44. A. J. Sparks, C. M. Smith, A. B. Allman, *et al.*, "Compliant vascular models 3D printed with the Stratasys J750: a direct characterization of model distensibility using intravascular ultrasound," 3D Print Med **7**(1), 28 (2021).
45. L. G. Lindberg, T. Tamura, and P. A. Oberg, "Photoplethysmography. Part 1. Comparison with laser Doppler flowmetry," Med. Biol. Eng. Comput. **29**(1), 40–47 (1991).
46. M. Nomoni, J. M. May, and P. A. Kyriacou, "A pulsatile optical tissue phantom for the investigation of light-tissue interaction in reflectance photoplethysmograph," in *2019 41st Annual International Conference of the IEEE Engineering in Medicine and Biology Society (EMBC)* (IEEE 2019), pp. 3204–3207.

Biomedical Optics EXPRESS

47. J. M. May, E. Mejía-Mejía, M. Nomoni, *et al.*, "Effects of contact pressure in reflectance photoplethysmography in an in vitro tissue-vessel phantom," Sensors **21**(24), 8421 (2021).
48. Y. Freile-Pelegrín, T. Madera-Santana, D. Robledo, *et al.*, "Degradation of agar films in a humid tropical climate: Thermal, mechanical, morphological and structural changes," Polym. Degrad. Stab. **92**(2), 244–252 (2007).
49. S. Chatterjee and P. A. Kyriacou, "Monte Carlo analysis of optical interactions in reflectance and transmittance finger photoplethysmography," Sensors **19**(4), 789 (2019).
50. S. A. Prahl, "Everything I think you should know about Inverse Adding-Doubling, Oregon Medical Laser Center," St. Vincent Hospital **1**, 1–74 (2011).
51. A. Committee, "Standard test methods for vulcanized rubber and thermoplastic rubbers and thermoplastic elastomers-Tension [D412-98]," New York: American National Standards Institute (1998).
52. M. A. Goda, P. H. Charlton, and J. A. Behar, "pyPPG: A Python toolbox for comprehensive photoplethysmography signal analysis," arXiv arXiv:2309.13767 (2023).
53. Q. Li and G. D. Clifford, "Dynamic time warping and machine learning for signal quality assessment of pulsatile signals," Physiol. Meas. **33**(9), 1491–1501 (2012).
54. M. Elgendi, "Optimal signal quality index for photoplethysmogram signals," Bioengineering **3**(4), 21 (2016).
55. R. Sahni, "Noninvasive monitoring by photoplethysmography," Clin. Perinatol. **39**(3), 573–583 (2012).
56. M. Liu, J. Sun, and Q. Chen, "Influences of heating temperature on mechanical properties of polydimethylsiloxane," Sens. Actuators, A **151**(1), 42–45 (2009).
57. I. D. Johnston, D. K. McCluskey, C. K. Tan, *et al.*, "Mechanical characterization of bulk Sylgard 184 for microfluidics and microengineering," J. Micromech. Microeng. **24**(3), 035017 (2014).